

The cold origin of the warm dust around ε Eridani

M. Reidemeister¹, A. V. Krivov¹, C. C. Stark², J.-C. Augereau³, T. Löhne¹, and S. Müller¹

¹ Astrophysikalisches Institut, Friedrich-Schiller-Universität Jena, Schillergäßchen 2–3, 07745 Jena, Germany
e-mail: martin.reidemeister@astro.uni-jena.de

² Department of Physics, University of Maryland, Box 197, 082 Regents Drive, College Park, MD 20742-4111, USA

³ Laboratoire d'Astrophysique de Grenoble, CNRS UMR 5571, Université Joseph Fourier, Grenoble, France

Received 2 July 2010 / Accepted 27 October 2010

ABSTRACT

Context. The nearby K2 V star ε Eridani hosts one known inner planet, an outer Kuiper belt analog, and an inner disk of warm dust. *Spitzer*/IRS measurements indicate that the warm dust is present at distances as close as a few AU from the star. Its origin is puzzling, since an “asteroid belt” that could produce this dust would be unstable because of the known inner planet.

Aims. Here we test a hypothesis that the observed warm dust is generated by collisions in the outer belt and is transported inward by Poynting-Robertson drag and strong stellar winds.

Methods. We simulated a steady-state distribution of dust particles outside 10 AU with a collisional code and in the inner region ($r < 10$ AU) with single-particle numerical integrations. By assuming homogeneous spherical dust grains composed of ice and astrosilicate, we calculated the thermal emission of the dust and compared it with observations. We investigated two different orbital configurations for the inner planet inferred from radial velocity measurements, one with a highly eccentric orbit of $e = 0.7$ and another one with a moderate eccentricity of $e = 0.25$. We also produced a simulation without a planet.

Results. Our models can reproduce the shape and magnitude of the observed spectral energy distribution from mid-infrared to submillimeter wavelengths, as well as the *Spitzer*/MIPS radial brightness profiles. The best-fit dust composition includes both water ice and silicates. The results are similar for the two possible planetary orbits and without a planet.

Conclusions. The observed warm dust in the ε Eridani system can indeed stem from the outer “Kuiper belt” and be transported inward by Poynting-Robertson and stellar wind drag. The inner planet has little effect on the distribution of dust, so that the planetary orbit could not be constrained. Reasonable agreement between the model and observations can only be achieved by relaxing the assumption of purely silicate dust and assuming a mixture of silicate and water ice in comparable amounts.

Key words. planets and satellites: formation – circumstellar matter – stars: individual: ε Eridani – planet-disk interactions – zodiacal dust

1. Introduction

The nearby (~ 3.2 pc) K2 V star ε Eridani (HD 22049, HIP 16537, HR 1084), with an age of $\lesssim 1$ Gyr (Saffe et al. 2005; Di Folco et al. 2004; Song et al. 2000; Soderblom & Dappen 1989), has a ring of cold dust at ~ 65 AU seen in resolved submillimeter images (Greaves et al. 1998, 2005), which encompasses an inner disk of warm dust revealed by *Spitzer*/MIPS (Backman et al. 2009). The star is orbited by a radial velocity planet (Hatzes et al. 2000) with a semimajor axis of 3.4 AU. Another outer planet may orbit near ~ 40 AU, producing the inner cavity and clumpy structure in the outer ring (Liou & Zook 1999; Ozernoy et al. 2000; Quillen & Thorndike 2002; Deller & Maddison 2005). The excess emission at $\lambda \gtrsim 15 \mu\text{m}$ in the *Spitzer*/IRS-spectrum (Backman et al. 2009) indicates that there is warm dust close to the star, at a few AU (inset in Fig. 1). Its origin is unknown, as an inner “asteroid belt” that could produce this dust would be dynamically unstable because of the known inner planet (Brogi et al. 2009).

Here, we check the possibility that the source of the warm dust is the outer ring from which dust grains could be transported inward by Poynting-Robertson drag and stellar wind. The importance of the latter for debris disks around late-type, low-mass stars was first pointed out by Plavchan et al. (2005), and it is well known that ε Eridani does have strong winds (Wood et al. 2002).

It is convenient to divide the entire system into three regions: the outer “Kuiper belt” (55–90 AU), the intermediate zone (10–55 AU), and the inner region (inside 10 AU), see Fig. 1. In Sect. 2 we describe the modeling setup. In Sect. 3 we model the dust production in the outer ring and its transport through the intermediate region. Section 4 describes simulations of the inner system. Section 5 presents the spectral energy distribution (SED) modeling and provides an additional check for connection between the inner system and the outer parent ring (Sect. 5.4). Section 6 focuses on the surface brightness profiles. Section 7 contains our conclusions.

2. Model setup

2.1. Method

Our model includes gravitational forces from the star and an inner planet, radiation and stellar wind pressure, drag forces induced by both stellar photons and stellar wind particles (Burns et al. 1979), as well as collisions. Dust production in the outer region and dust transport through the intermediate region are modeled with a statistical collisional code. To study the dust in the inner region, we need to handle dust interactions with the inner planet. These cannot be treated by the collisional code, so we model the inner region by collisionless numerical integration.

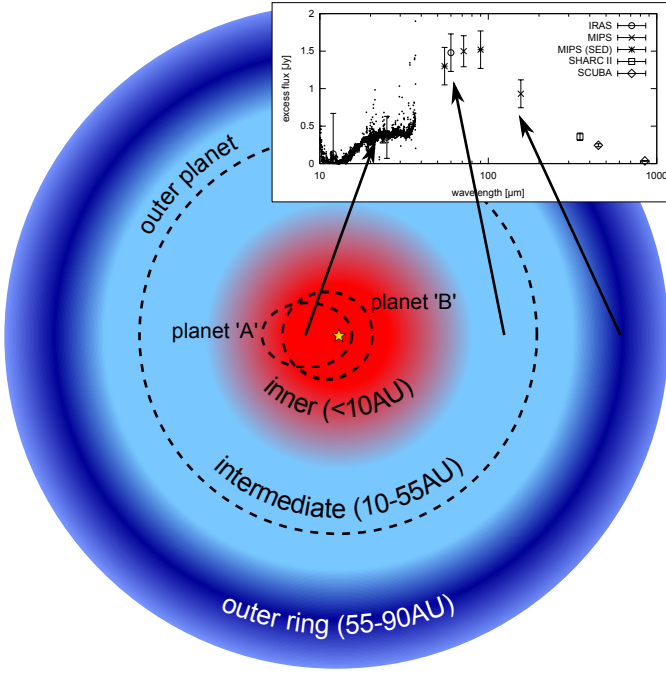


Fig. 1. A schematic view of the ϵ Eridani system’s architecture. The outer ring is the region where the dust is produced by parent planetesimals; the intermediate zone is the one where it is transported inward by drag forces, possibly interacting with a presumed outer planet; transport continues through the inner region where dust interacts with the known inner planet. Two possible orbits of the inner planet are shown. The outer part of the sketch (>10 AU) is not to scale. *Inset:* the observed SED. The IRS spectrum (dots) stems from dust in the inner region and exhibits a characteristic “plateau” (“shoulder”) at $\lambda \approx 20\text{--}30\ \mu\text{m}$. The main part of the SED with a maximum at $\lambda \approx 70\text{--}80\ \mu\text{m}$, well probed by several photometry points (symbols with error bars), derives from the outer and intermediate regions.

2.2. Stellar properties

We assumed a stellar mass of $M_{\star} = 0.83 M_{\odot}$ (Benedict et al. 2006) and a luminosity of $L_{\star} = 0.32 L_{\odot}$ (Di Folco et al. 2007). For the stellar spectrum we used a NextGen model (Hauschildt et al. 1999) with an effective temperature of 5200 K, $\log g = 4.5$, solar metallicity, and stellar radius $R_{\star} = 0.735 R_{\odot}$ (Di Folco et al. 2007).

2.3. Dust grain properties

The knee in the IRS spectrum at $\sim 20\ \mu\text{m}$ (inset in Fig. 1) is reminiscent of a classical silicate feature. Since the exact composition of those silicates is not known, we have chosen astronomical silicate (Laor & Draine 1993) ($\rho_d = 3.5\ \text{g cm}^{-3}$). On the other hand, by analogy with the surface composition of Kuiper belt objects in the solar system (e.g., Barucci et al. 2008), we may expect many additional species such as ices and organic solids. In particular, it is natural to expect water ice to be present, especially given that the source of dust is a “Kuiper belt” located very far from the star ($\sim 55\text{--}90$ AU), and the star itself has a late spectral class. Accordingly, we also tried homogeneous mixtures of astrosilicate with 50% and 70% volume fraction of water ice (Li & Greenberg 1998) ($\rho_d = 1.2\ \text{g cm}^{-3}$). The bulk density of these ice-silicate mixtures is $\rho = 2.35\ \text{g cm}^{-3}$ and $\rho = 1.89\ \text{g cm}^{-3}$, respectively. The optical constants of the mixtures were calculated by effective medium theory with the Bruggeman mixing rule. In

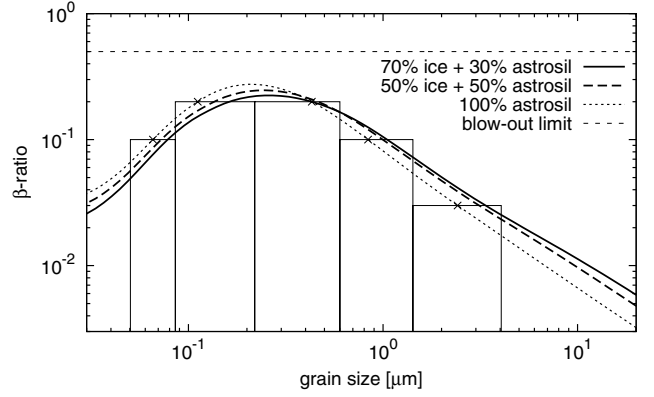


Fig. 2. The β ratio of two silicate – water ice mixtures, compared to a pure silicate composition, as a function of size for ϵ Eri. The bars show the size bins used in the inner disk simulations (Sect. 4). The dashed horizontal line shows the dynamical blowout limit of $\beta = 0.5$.

all three cases (pure astrosilicate, two ice-silicate mixtures) the dust grains were assumed to be compact spheres.

2.4. Radiation pressure

Using the optical constants and adopting Mie theory, the radiation pressure efficiency Q_{rp} , averaged over the stellar spectrum, was calculated as a function of size s (Burns et al. 1979; Gustafson 1994). We then computed the radiation pressure to gravity ratio, β (Fig. 2). The resulting $\beta(s)$ was utilized to compute the direct radiation pressure and Poynting-Robertson forces.

2.5. Stellar wind

The stellar wind was included by a factor β_{sw}/β , which is the ratio of stellar wind pressure to radiation pressure:

$$\frac{\beta_{\text{sw}}}{\beta} = \frac{F_{\text{sw}}}{F_{\text{rp}}} = \frac{\dot{M}_{\star} v_{\text{sw}} c}{L_{\star}} \frac{Q_{\text{sw}}}{Q_{\text{rp}}}, \quad (1)$$

where Q_{sw} is the efficiency factor for stellar wind pressure (Burns et al. 1979; Gustafson 1994). We adopted $Q_{\text{sw}} = 1$. Assuming a stellar wind velocity equal to the average solar wind velocity, $v_{\text{sw}} \approx 400\ \text{km s}^{-1}$, and using a mass-loss rate of $\dot{M}_{\star} \approx 30 \dot{M}_{\odot}$ (Wood et al. 2002), we get $\beta_{\text{sw}} = 3.69 \times 10^{-2} \beta$. In this estimate (but not in the simulations), we set Q_{rp} to unity. Thus direct stellar wind pressure is approximately 27 times weaker than radiation pressure. However, the stellar wind drag is $(\beta_{\text{sw}}/\beta)(c/v_{\text{sw}}) \approx 28$ times stronger than radiation (Poynting-Robertson) drag.

2.6. Sublimation

Using an ice-silicate mixture for dust raises a question whether and where the icy portion of the dust grains will suffer sublimation. The ice sublimation temperature of ~ 100 K (e.g. Moro-Martín & Malhotra 2002; Kobayashi et al. 2008) is reached at ≈ 10 AU (Fig. 3). Mukai & Fechtig (1983) proposed that fluffy and nearly homogeneous grains of ice and silicates can produce a core of silicate after sublimation of ice. Assuming a grain with a volatile icy mantle, instead of a homogeneous sphere of ice and silicates, would lead to the same result. In both cases, the silicate cores left after ice sublimation continue to drift

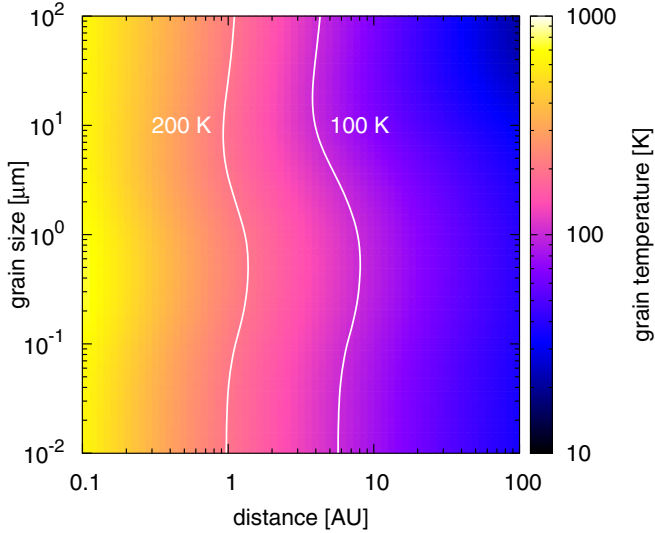


Fig. 3. Equilibrium grain temperature of an 70% ice and 30% astronomical silicate composition depending on grain size s and distance to the star r . The results for the 50% ice – 50% silicate mixture are similar. The wavy shape of the isotherms is caused by the dependence of the absorption efficiency on the grain size (as explained in Krivov et al. 2008, see their Figs. 2 and 6).

further inward. Within the ice sublimation distance, the optical depth would decrease by the volume fraction of the refractories (see Kobayashi et al. 2008, their Eq. (35)). The shape of the size distribution is not affected by sublimation, as long as the volume fraction of ice is independent of the grain size.

Thus we expect the entire dust disk to consist of an inner silicate disk ($r \lesssim 10$ AU) and an outer disk of an ice-silicate composition. Accordingly, in integrations described in Sect. 4 we assumed dust inside 10 AU to consist of pure astrosilicate. Outside 10 AU, we tried all three dust compositions described above.

We finally note that a ring due to sublimation as described in Kobayashi et al. (2008, 2009) is not expected, because such a ring can only be produced by particles with high β ratios ($\beta \gtrsim 0.1$ –0.3). Such β ratios are barely reached in the ε Eri system even for pure silicate dust.

3. Dust in the outer and intermediate regions

3.1. Model

We used our statistical collisional code *ACE* (*Analysis of Collisional Evolution*) (Krivov et al. 2005, 2006; Löhne et al. 2008) to model the collisional disk beyond 10 AU. This includes the parent ring near 65 AU (Greaves et al. 2005) and the intermediate region inside it. The *ACE* simulation provides us with a rotationally-symmetric steady-state dust size distribution at 10 AU, which we use later as input for our non-collisional models of the inner disk (see Sect. 4). The code is not able to treat planetary perturbations. Thus we neglect the presumed outer planet, but will qualitatively discuss its possible influence in Sects. 3.2 and 5.

We made three *ACE* runs, assuming the dust composition to be pure astrosilicate, a mixture of ice and astrosil in equal parts, and a mixture of 70% ice and 30% astrosil, as described above. In handling the collisions, the critical specific energy for

fragmentation and dispersal Q_D^* is calculated by the sum of two power laws,

$$Q_D^* = A_s \left(\frac{s}{1 \text{ m}} \right)^{3b_s} + A_g \left(\frac{s}{1 \text{ km}} \right)^{3b_g}, \quad (2)$$

where the first and the second terms account for the strength and the gravity regimes, respectively. We took the values $A_s = 10^7 \text{ erg g}^{-1}$, $A_g = 10^7 \text{ erg g}^{-1}$, $3b_s = -0.37$, and $3b_g = 1.38$ (cf. Benz & Asphaug 1999). In all *ACE* runs, we assumed that the outer ring has a uniform surface density between 55 and 90 AU and that the eccentricities of parent planetesimals range between 0.0 and 0.05, and arbitrarily set the semi-opening angle of the disk to 3° . Next, we assumed that the *initial* size distribution index of solids from km-sized planetesimals down to dust is $q \sim 3.6$ (see, e.g. Löhne et al. 2008, for a justification of this choice). The current dust mass was set to $\mathcal{M}(s < 1 \text{ mm}) \approx 10^{-3} \mathcal{M}_\oplus$, based on previous estimates from sub-millimeter images (Greaves et al. 1998, 2005).

3.2. Results

Figure 4 (left) shows the resulting size distribution in an *evolved* disk at several distances from the star. It shows the case of a mixture of 70% ice and 30% astrosil, but the results for the two other compositions are qualitatively similar. We start a discussion of it with the parent ring (55–90 AU). For grains larger than $s_c \approx 10 \mu\text{m}$, the differential size distribution has a slope $q \approx 3.7$. Since Fig. 4 (left) plots the optical depth τ per size decade, this corresponds to a slope of $q - 3 = -0.7$. This is close to what is expected theoretically for collision-dominated disks (Dohnanyi 1969). However, from $s_c \approx 10 \mu\text{m}$ down to the smallest grains, the size distribution flattens, because the inward drift is faster for smaller grains – or, more exactly, for grains with higher β -ratios (see, e.g., Strubbe & Chiang 2006; Vitense et al. 2010, for a more detailed discussion of this phenomenon). The slope calculated analytically for a transport-dominated disk with $\beta \propto s^{-1}$ is $q \approx 2.5$. The actual size distribution is wavy, and is rather close to $q = 3.0$, which would correspond to a uniform distribution of the optical depth across the sizes. One reason for that is a nonlinear dependence of β on the reciprocal of particle size (Fig. 2).

Closer to the star, the slope for big grains progressively steepens because of their preferential collisional elimination. At the same time, the break s_c in the size distribution moves to smaller sizes. Already at 20 AU, particles larger than $\sim 10 \mu\text{m}$ are almost absent. At 10 AU, the cutoff shifts to $s \sim 4 \mu\text{m}$. We argue that a progressive depletion of larger grains with decreasing distance will be strengthened further by the alleged outer planet at 40 AU. That planet, which presumably sculpts the outer ring, would stop bigger grains more effectively than smaller ones, by trapping some of them in mean-motion resonances (MMRs) and scattering the others (Liou et al. 1996; Moro-Martín & Malhotra 2003; Moro-Martín & Malhotra 2005). As a result, we do not expect any grains larger than about 1–10 μm ($\beta \lesssim 0.1$ –0.01) throughout most of the intermediate zone and in the entire inner region. At the same time, the outer planet is not expected to be an obstacle for smaller particles that, as discussed below, will be the most important for the mid-IR part of the SED.

From the same *ACE* run for the outer and intermediate regions, we found that τ is nearly constant from 55 AU down to 10 AU (Fig. 4 right). This optical depth is dominated by submicron-sized and micron-sized grains. A constant optical depth inward from the sources is known to be a characteristic feature of transport-dominated disks (e.g. Briggs 1962;

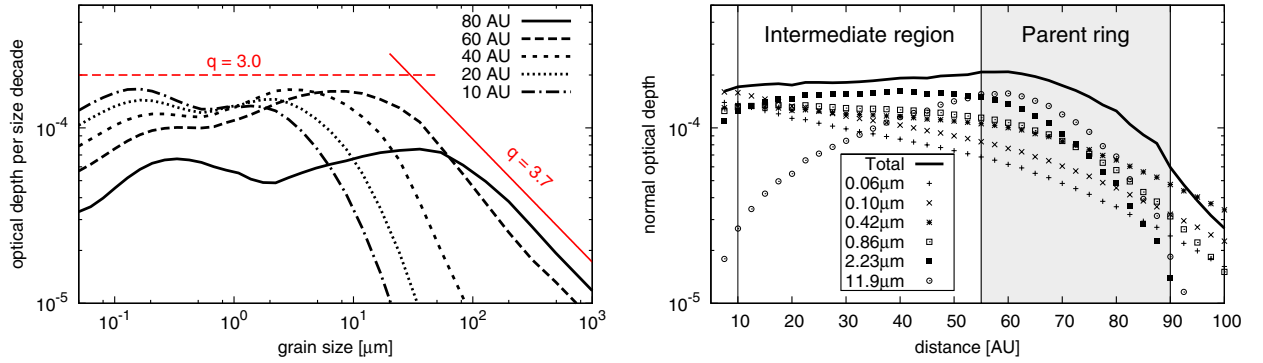


Fig. 4. *Left:* size distribution at different distances in a disk composed of 70% ice and 30% silicate, simulated with *ACE*. Curves depict the normal geometrical optical depth per size decade, as a function of size. The straight lines show power laws with $q = 3.0$ and 3.7 for comparison. (Their height is arbitrary.) *Right:* radial profiles of the optical depth. Symbols: partial contributions to the optical depth by several selected sizes. Each contribution is normalized to the unit size decade around that size. Solid line: the total optical depth of the disk.

Wyatt 2005). However, disks with the optical depth of $\tau \gtrsim 10^{-5}$ are usually thought to be collision-dominated (Wyatt 2005), and one might not expect that even the amplification of the Poynting-Robertson drag by stellar wind drag would increase the critical optical depth (that separates the transport- and collision-dominated regimes) by more than an order of magnitude. This raises a natural question: how can it be that a disk with the optical depth of $\sim 2 \times 10^{-4}$ is transport-dominated? To find an answer, we note that s_c discussed above is a critical grain size, for which the collisional lifetime is equal to the characteristic inward drift timescale. Therefore, the disk is collision-dominated at $s > s_c$ and transport-dominated at $s < s_c$. In the “usual” disks, increasing τ would sooner or later force s_c to reach the radiation pressure blowout limit s_{blow} . At that value of τ , the entire disk becomes collision-dominated, since there is very little material in the disk of size $s < s_{\text{blow}}$. But not in the ϵ Eri disk! Here, the blowout limit does not exist (Fig. 2). Therefore, for any reasonable size distribution ($q \geq 3$), the optical depth is dominated by small particles with $s < s_c$, and these are in the transport-dominated regime. That is why our simulation shows that the outer and intermediate regions of the ϵ Eri disk is dominated by grains roughly in the $0.05\text{--}1\ \mu\text{m}$ size range and, at those sizes, is nearly collisionless, despite τ of $\sim 10^{-4}$. The same conclusion holds, of course, for the inner disk inside 10 AU. For this reason, we believe our model of the inner disk in the following section, which is obtained via collisionless numerical integration, is appropriate.

4. Dust in the inner region

4.1. Model

To investigate the behavior of dust in the inner region ($r < 10$ AU) of the ϵ Eri debris disk and its interaction with the inner planet, we performed numerical integrations of grain trajectories. We used a Burlisch-Stoer algorithm (Press et al. 1992). Collisions are not considered in our inner disk model, because, as shown above, they play a minor role in the inner disk.

The dust grains were treated as massless particles, described only by their β ratio (or sizes) and their orbital elements: semi-major axis a , eccentricity e , inclination i , longitude of ascending node Ω , argument of pericenter ω , and mean anomaly M .

In our simulations we examined the following grain sizes s_i ($i = 1, \dots, 5$): 0.07 , 0.11 , 0.43 , 0.84 , and $2.42\ \mu\text{m}$. These correspond to the β ratios of $\beta_i = 0.1, 0.2, 0.2, 0.1,$ and 0.03 , respectively (Fig. 2). Each s_i represents a size interval ($\delta s_i, \hat{s}_i$). The

limits of these intervals are set to the middle of s_i and the adjacent sizes s_{i-1} and s_{i+1} (in logarithmic scale). Since, due to the low luminosity of the central star, the blowout grain size does not exist, the lower cut-off for the particle sizes was arbitrarily set to $\delta s_1 = 0.05\ \mu\text{m}$. Smaller particles are not expected to contribute significantly to the SED at mid-IR and longer wavelengths. In addition, we expect that various erosive effects (e.g., plasma sputtering) and dynamical effects (e.g., the Lorentz force), which are not included in our model, would swiftly eliminate the tiniest grains from the system. Particles larger than $\hat{s}_5 = 4\ \mu\text{m}$ are not considered in these simulations, because they are absent in this region (cf. Fig. 4, right).

Since grains with the same β ratios experience the same force, it was enough to run three simulations ($\beta_i = 0.2, 0.1,$ and 0.03) to cover all five grain sizes. We used 10000 particles for each value of β . The grains were placed in orbits with initial eccentricities from 0 to 0.3 and an initial semimajor axis of $20\ \text{AU}$ ¹, assuming that they have passed the expected outer planet and are out of the range of its perturbation. The rather high initial eccentricities of up to 0.3 were taken, because these are expected to be increased by perturbations of the outer planet when passing through its orbit. The initial inclinations were uniformly distributed between 0° and 10° , respectively. The angular elements (Ω, ω, M) were all uniformly distributed between 0° and 360° .

For the inner planet we used two different orbital configurations. These configurations fit the observations from Benedict et al. (2006) and Butler et al. (2006), in the following called cases “A” and “B”, respectively. In both cases we set the planet’s semimajor axis to $3.4\ \text{AU}$ and assumed its orbit to be co-planar with the disk’s mid-plane. Benedict et al. (2006) estimate the planet’s mass and eccentricity to $M_{P_A} = 0.78\ M_{\text{Jup}}$ and $e_{P_A} = 0.7$, while Butler et al. (2006) give $M_{P_B} = 1.06\ M_{\text{Jup}}$ and $e_{P_B} = 0.25$. We also produced a simulation without an inner planet. A summary of the initial parameters for the simulations is given in Table 1.

4.2. Results

From our simulations we created a radial profile of the normal geometrical optical depth, assuming a steady-state distribution (Fig. 5). It illustrates that the inner planet intercepts a fraction of

¹ We use 20 AU instead of 10 AU because, if we placed the particles at 10 AU with eccentricities from 0 to 0.3, the initial distances would be distributed between 7 and 13 AU, causing an unwanted “boundary effect” of decreased optical depth in that distance range.

Table 1. Initial parameters of the inner disk simulations.

| Star | | |
|---------------------------|--|---------------------------------|
| M_\star | $0.83 M_\odot$ | |
| L_\star | $0.32 L_\odot$ | |
| \dot{M}_\star | $30 \dot{M}_\odot = 6 \times 10^{-13} M_\odot \text{ yr}^{-1}$ | |
| v_{sw} | 400 km s^{-1} | |
| planet | | |
| M_P | A $1.78 \times 10^{-3} M_\star$ | B $2.44 \times 10^{-3} M_\star$ |
| a_P | 3.4 AU | 3.4 AU |
| e_P | 0.7 | 0.25 |
| i_P | 0.0° | 0.0° |
| M_P, Ω_P, ω_P | 0.0° | 0.0° |
| dust | | |
| β | 0.2, 0.1, 0.03 | |
| a_0 | 20 AU | |
| e_0 | [0.0, 0.3] | |
| i_0 | [0° , 10°] | |
| M_0, Ω_0, ω_0 | [0° , 360°] | |

Notes. A range of $[a, b]$ indicates that the parameters are equally distributed between a and b , and randomly chosen.

dust on its way inward by capturing the grains in MMRs and/or scattering those grains that pass the planetary orbit. This results in an inner gap around and inside the planet orbit. The gap is deeper for grains with smaller β ratios, because they drift inward more slowly, which increases the probability of a resonance trapping or a close encounter with the planet. Another conclusion from Fig. 5 is that the radial profiles in the cases “A” and “B” do not differ much, although the eccentricities of planetary orbits are quite different.

5. Spectral energy distribution

5.1. SED from the outer and intermediate regions

Having calculated the distribution of dust particles with different β ratios in the ε Eridani system, we need to calculate the thermal emission of the dust for comparison with the observed SED. We start with the SED of the outer and intermediate region together. We have calculated it, using the output of the ACE runs described in Sect. 3. Specifically, coupled radial and size distributions of dust between 10 and 90 AU shown in Fig. 4 were used.

The results are shown in Fig. 6. Overplotted are the data points, all taken from Fig. 7 of Backman et al. (2009); see also their Table 1. Clearly, the model with 100% astrosilicate contents is too “warm”. Notably, the SED starts to rise towards the main maximum too early (at $\approx 25 \mu\text{m}$ instead of $\approx 35 \mu\text{m}$), which is inconsistent with the “plateau” of the IRS spectrum. Including 50% ice improves the model, but the SED still rises too early. The best match of the data points is achieved with a 30% astrosil and 70% ice mixture, which will therefore be used in the rest of the paper. Still, even for that mixture, the main part of the SED (i.e. the combined contribution of the outer ring and the intermediate region) predicted by the collisional model is somewhat “warmer” than it should be. We discuss this slight discrepancy in Sect. 5.3.

5.2. SED from the inner region

We now consider an SED coming from dust in the inner disk. The optical constants, density of the dust, and the stellar spectrum described in Sect. 2.3 have been used to calculate the “partial” SEDs from each grain size bin. To sum up the contributions

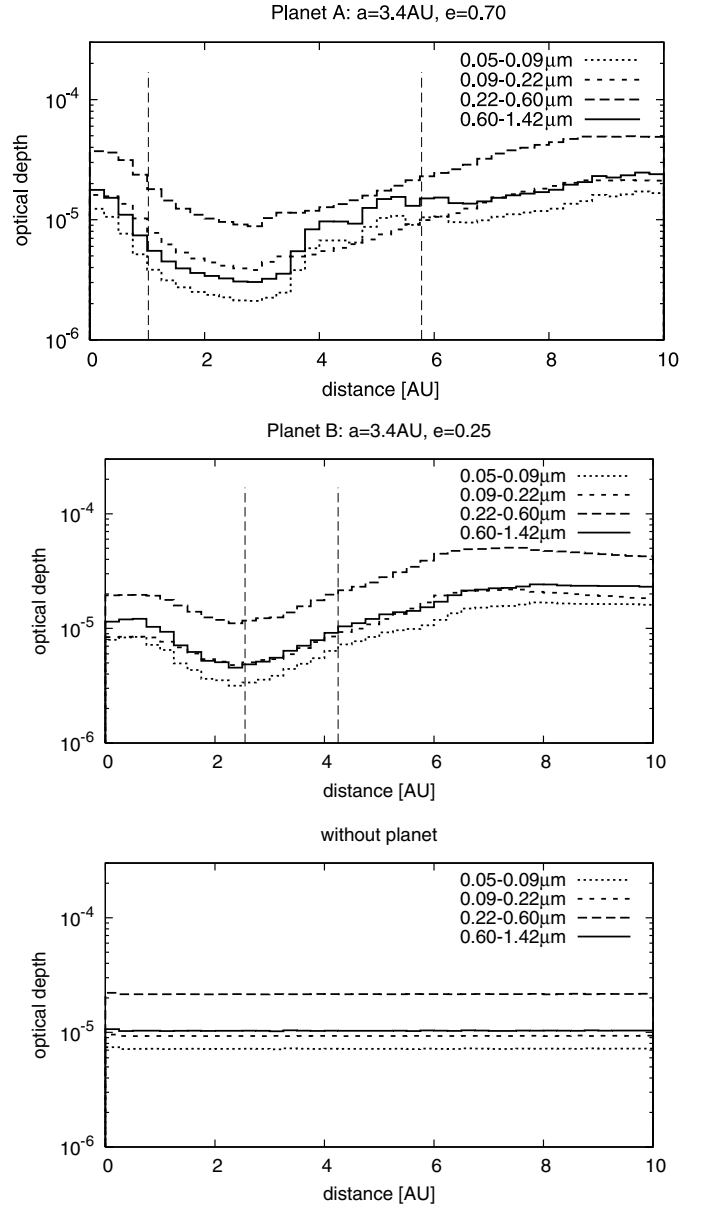


Fig. 5. Radial profile of the normal geometrical optical depth produced by different grain size bins for the planet “A” (top), “B” (middle), and without a planet (bottom). A radial bin width is $\Delta r = 0.25$ AU. Vertical dashed lines show periastron and apastron of the planet orbit. A size distribution with a slope of $q = 3.0$ and the dust mass of $M_{\text{dust}} \approx 8.5 \times 10^{-8} M_\oplus$ (case “A”), $9.9 \times 10^{-8} M_\oplus$ (case “B”), and $5.6 \times 10^{-8} M_\oplus$ (without a planet) were used for the vertical scaling of the curves.

from different bins, we assumed a power law $M(s)ds \propto s^{-q}ds$. There are two parameters that allow us to adjust the resulting SED of the inner region to the IRS spectrum. One is the slope q that provides a “weighting” of relative contributions of different-sized grains into the resulting SED. In accord with our results in Sect. 3.2, we take $q = 3$ and only consider grains with $s \leq 2 \mu\text{m}$ (four lowest size bins). Another parameter should characterize the absolute amount of dust in the inner region. (This could be, for instance, the total dust mass in the inner region.) This parameter would determine the overall height of the SED. We varied the dust mass until the resulting model SED fits the IRS spectrum best. The best results were achieved with the total dust mass in the inner region of $M_{\text{dust}} \approx 8.5 \times 10^{-8} M_\oplus$ in the case “A”, $9.9 \times 10^{-8} M_\oplus$ in the case “B”, and $5.6 \times 10^{-8} M_\oplus$ without a

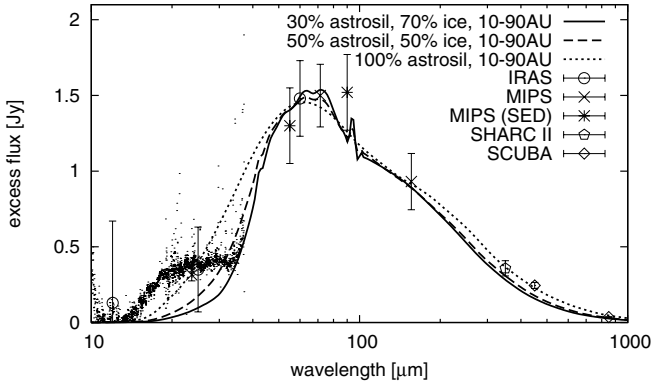


Fig. 6. The SED from dust outside 10 AU in the ϵ Eri dust disk. Symbols with error bars are data points and scattered dots are the IRS spectrum. Lines are model SEDs for different dust compositions: 100% astrosil (dotted), 50% ice and 50% astrosil (dashed), and 70% ice and 30% astrosil (solid).

planet. The absolute height of optical depth profiles from various size bins shown in Fig. 5 corresponds to the same dust masses and the same slope $q = 3.0$.

Figure 7 shows the contribution of the different grain sizes to the SED and their total. We now use a logarithmic scale. Although the two planet orbits are quite different, the influence of the planet on the SED is rather minor, because the radial distributions of dust are similar in both cases.

A consistency check that we made was to compare the model predictions with the results of interferometric measurements with CHARA array in the K -band ($2.2 \mu\text{m}$) (Di Folco et al. 2007). They set the upper limit of the fractional excess emission of the inner debris disk to 6×10^{-3} (3σ upper limit). With the photospheric flux of 120 Jy at $\lambda = 2.2 \mu\text{m}$, this translates to an excess of $\lesssim 720 \text{ mJy}$. This value includes both thermal emission and scattered light. The integrated surface brightness of the $2.2 \mu\text{m}$ radial thermal emission profile, convolved with the CHARA transmission profile, generates a total excess of just 25.7 mJy , 14.5 mJy , and 15.4 mJy for the cases “A”, “B”, and without an inner planet, respectively. Even if we took scattered light into account, which we estimate contributes ≈ 3.4 times more than the thermal emission at that wavelength, our model would be consistent with non-detection of dust with CHARA.

5.3. SED from the entire disk

We now assemble the SED produced by the entire disk. To this end, we summed up the SEDs of the inner region and of the region outside 10 AU presented in Figs. 6 and 7, respectively. Figure 8 shows the complete SED. It is in a reasonable, although not a perfect, agreement with the observations. In particular, the maximum of the modeled SED, while reproducing the data points within their error bars, appears to lie at a slightly shorter wavelength than the one suggested by the data points. A likely reason for this discrepancy is that our collisional simulation does not take into account elimination of particles in the size range from ~ 1 to $\sim 100 \mu\text{m}$ by the alleged outer planet, as explained above. Excluding these particles from the intermediate region $10\text{--}55 \text{ AU}$ would reduce emission in the $35\text{--}70 \mu\text{m}$ wavelength range, shifting the maximum of the SED to a longer wavelength. In addition, the main part of the SED can be made “colder” by varying diverse parameters of the collisional simulation, many of which are not at all or are poorly constrained.

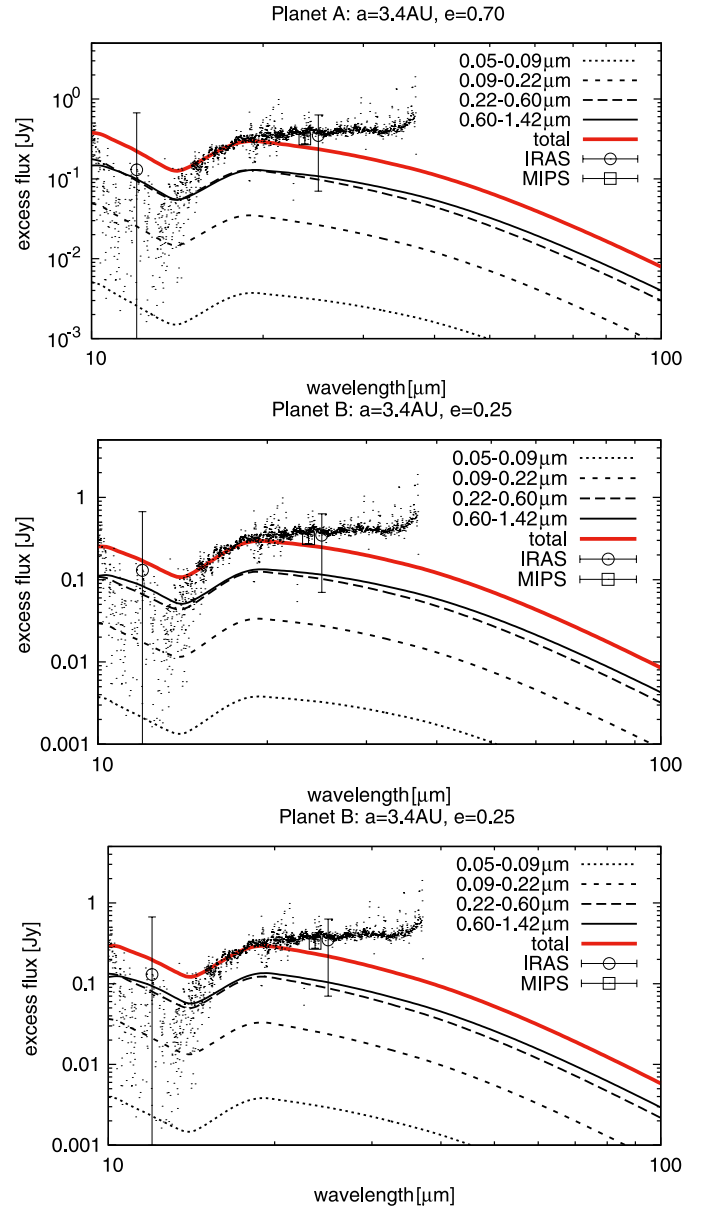


Fig. 7. The observed *Spitzer*/IRS spectrum (Backman et al. 2009) (small dots) and the modeled SED of the inner region. *Top*: planet “A”, *middle*: planet “B”, *bottom*: without a planet. Thin lines: contributions of the different size bins to the SED, thick line: the total emission from all sizes. The size distribution slope q and the dust mass M_{dust} are the same as in Fig. 5.

These include the eccentricity distribution of planetesimals, the opening angle of the planetesimal disk, as well as the mechanical strength of solids. Such a search for the best fit would, however, be very demanding computationally. We deem the fit presented in Fig. 8 sufficiently good to demonstrate that our scenario, in which inner warm dust is produced in the outer ring, is feasible.

5.4. Connecting outer and inner regions

To make sure that the amount of dust required to reproduce the IRS spectrum is consistent with the amount of dust that could be supplied to the inner disk from the outer parent belt, we now make an important consistency check. From calculations of the dust production in the outer ring and its transport through the intermediate region, we know the optical depth at 10 AU. Figure 4

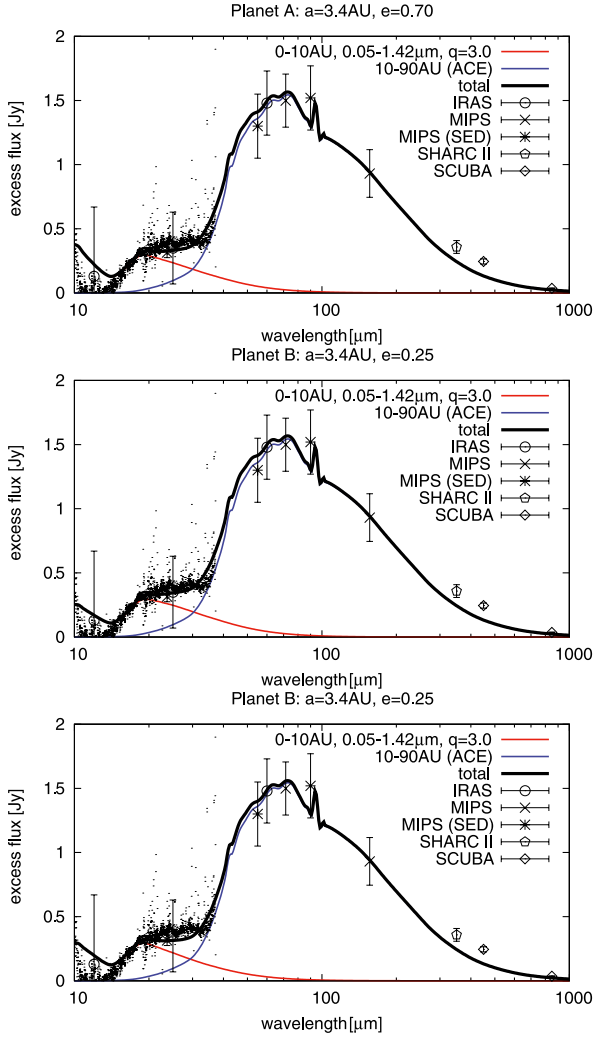


Fig. 8. The entire SED of the ε Eri dust disk. Symbols with error bars are data points, small dots is the IRS spectrum. Thick line in each panel is the excess emission predicted by the models, and thin lines show contributions from the inner region (<10 AU) and the intermediate+outer disk. Three panels are for the planet configurations “A” (top), “B” (middle), and without a planet (bottom).

(right) suggests that the optical depth per size decade, created by grains with sizes of 0.07, 0.11, 0.43, and 0.84 μm , is about $(1-2) \times 10^{-4}$. These values have to be compared with optical depths, sufficient to reproduce the IRS spectrum. From Fig. 5 outside the planetary region we read out the values $(2-5) \times 10^{-5}$ for the four lowest size bins (which are centered on the same four grain sizes). Taking into account the actual width of the four lowest size bins used in the modeling of the inner system, which is ≈ 0.4 dex, we would need an optical depth per size decade of $(5-10) \times 10^{-5}$. Thus the optical depth that is supplied by grains transported from outside matches the optical depth required to account for the IRS spectrum within a factor of two.

6. Surface brightness profiles

The model developed in this paper was designed to explain the *Spitzer*/IRS spectrum of the system. Besides this, we have made sure that it reproduces the entire SED probed with many instruments at the far-IR and sub-mm wavelengths. We now provide a comparison with other measurements that we have not considered before.

The most important information comes from spatially resolved images. *Spitzer*/MIPS observations yielded brightness profiles in all three wavelength bands centered on 24, 70, and 160 μm (Backman et al. 2009). We calculated the brightness profiles of thermal emission with our model. In doing so, we included both the outer+intermediate disk and the inner one. The resulting brightness profiles were convolved with the instrumental PSF (see Sect. 2 in Müller et al. 2010, for the algorithm used) and compared them with observed profiles.

The results are presented in Fig. 9. We only show case “A”, since the profiles in case “B” and without a planet are very similar. At all three wavelengths, the modeled brightness monotonically increases toward the star, as does the observed brightness. Both the slopes and the absolute brightness level are in good agreement with observations. The only exception is the modeled 70 μm profile (Fig. 9 middle). It is flatter than the observed one, predicting the brightness inside 30 AU correctly but overestimating the emission in most of the intermediate and the parent ring regions by a factor of two. The reasons for this deviation are probably the same as those discussed in Sect. 5.3. First, if a presumed outer planet at ≈ 40 AU efficiently eliminates particles in a size range from several to several tens of micrometers (which is not taken into account in our ACE simulations), this will decrease the 70 μm brightness in the intermediate region. Second, it should be possible to slightly decrease the 70 μm emission in the parent ring region by varying poorly known parameters in the collisional simulation.

We also checked the radial brightness profile at 850 μm and compared it with JCMT/SCUBA observations (Greaves et al. 1998, 2005). After convolution with a Gaussian PSF of $\sigma = 5''$, the resulting profile is consistent with Greaves et al. (2005, their Fig. 2), showing a broad ring around ≈ 60 AU and a resolved central cavity.

7. Conclusions

In this paper we show that in the nearby system ε Eridani the *Spitzer*/IRS excess emission at $\lambda \sim 15-30 \mu\text{m}$ can be caused by dust that is produced in the known outer dust ring and that streams inward due to interaction with strong stellar winds.

By running a collisional code, we simulated the dust production in the outer ring between 55 AU and 90 AU with a dust mass of $10^{-3} M_{\oplus}$ and the subsequent transport of the dust inward to 10 AU. We then employed single-particle numerical integrations to simulate the dust transport further inward through the orbit of the known inner planet. The dust in the inner region was found to consist of grains smaller than $\approx 2 \mu\text{m}$, and the dust mass inside 10 AU was estimated to be $(6-10) \times 10^{-8} M_{\oplus}$. Combining the results of the collisional simulations outside 10 AU and numerical integrations inside that distance, we calculated the overall SED and radial brightness profiles. This SED is in a reasonable agreement with the available observational data, and it correctly reproduces the shape and the height of the *Spitzer*/IRS spectrum. Likewise, the brightness profiles are consistent with the *Spitzer*/MIPS data.

The best results are obtained with an ice-silicate composition (Laor & Draine 1993; Li & Greenberg 1998) of dust outside the ice sublimation distance of ≈ 10 AU, and an inner disk of non-volatile silicate grains inside that distance.

With the aid of the modeled spectra and brightness profiles, it is not possible to distinguish between the different orbital solutions for the inner, radial velocity planet proposed by Benedict et al. (2006) or Butler et al. (2006). Although the planetary orbits

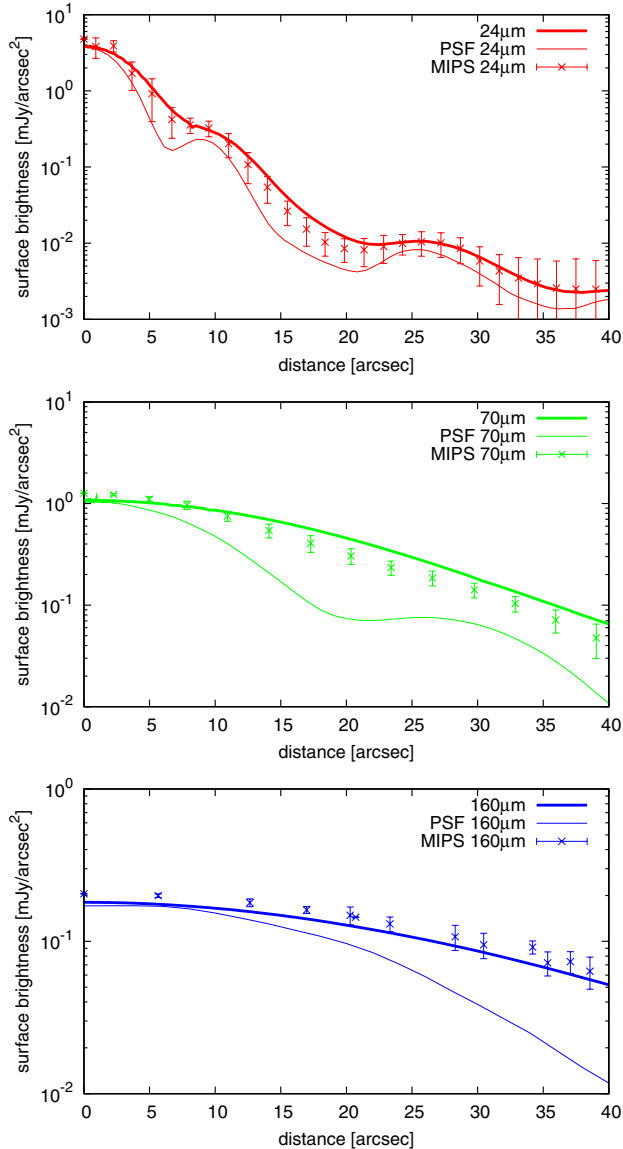


Fig. 9. Azimuthally averaged surface brightness profiles of the ϵ Eri dust disk (case “A”) at three *Spitzer*/MIPS wavelengths: $24\ \mu\text{m}$ (top), $70\ \mu\text{m}$ (middle), and $160\ \mu\text{m}$ (bottom). Points with error bars: star-subtracted MIPS data (Fig. 6 of Backman et al. 2009). Solid lines: modeled profiles after convolution with the PSFs. Thin solid lines: the instrumental PSF.

they inferred are quite different, both setups yield quite similar radial profiles of dust, the SEDs, and the brightness profiles.

Various kinds of new data on the ϵ Eri system are expected soon. Data from JCMT/SCUBA2 (Greaves, pers. comm.), *Herschel*/PACS, and *SPIRE* should shed light on the cold dust. This includes the structure of the outer “Kuiper belt” and the intermediate region of the disk between 10 and 55 AU. Furthermore, there is hope to better probe the inner warm dust directly, with instruments such as the Mid InfraRed Instrument (MIRI) aboard the upcoming James Web Space Telescope (JWST). Likewise, there is an ongoing effort to find outer planets in the system by direct imaging (Itoh et al. 2006; Marengo et al. 2006; Janson et al. 2007, 2008; Marengo et al. 2009).

Acknowledgements. We thank Johan Olofsson for assistance with reducing the *Spitzer*/IRS spectrum and Massimo Marengo and Karl Stapelfeldt for providing us with the *Spitzer*/MIPS brightness profiles. Useful discussions with Hiroshi Kobayashi are acknowledged. We appreciate critical readings of the manuscript by Philippe Thébault and by the anonymous reviewer. Part of this work was supported by the *Deutsche Forschungsgemeinschaft* (DFG), projects Kr 2164/8–1 and Kr 2164/9–1, by the *Deutscher Akademischer Austauschdienst* (DAAD), project D/0707543, and by the International Space Science Institute in Bern, Switzerland (“Exozodiacal Dust Disks and Darwin” working group²). SM was funded by the graduate student fellowship of the Thuringia State.

References

- Backman, D., Marengo, M., Stapelfeldt, K., et al. 2009, *ApJ*, 690, 1522
 Barucci, M. A., Brown, M. E., Emery, J. P., & Merlin, F. 2008, in *The Solar System Beyond Neptune*, ed. M. A. Barucci, H. Boehnhardt, D. P. Cruikshank, & A. Morbidelli, 143
 Benedict, G. F., McArthur, B. E., Gatewood, G., et al. 2006, *AJ*, 132, 2206
 Benz, W., & Asphaug, E. 1999, *Icarus*, 142, 5
 Briggs, R. E. 1962, *AJ*, 67, 710
 Brogi, M., Marzari, F., & Paolicchi, P. 2009, *A&A*, 499, L13
 Burns, J. A., Lamy, P. L., & Soter, S. 1979, *Icarus*, 40, 1
 Butler, R. P., Wright, J. T., Marcy, G. W., et al. 2006, *ApJ*, 646, 505
 Deller, A. T., & Maddison, S. T. 2005, *ApJ*, 625, 398
 Di Folco, E., Thévenin, F., Kervella, P., et al. 2004, *A&A*, 426, 601
 Di Folco, E., Absil, O., Augereau, J.-C., et al. 2007, *A&A*, 475, 243
 Dohnanyi, J. S. 1969, *J. Geophys. Res.*, 74, 2531
 Greaves, J. S., Holland, W. S., Moriarty-Schieven, G., et al. 1998, *ApJ*, 506, L133
 Greaves, J. S., Holland, W. S., Wyatt, M. C., et al. 2005, *ApJ*, 619, L187
 Gustafson, B. A. S. 1994, *Ann. Rev. Earth Plan. Sci.*, 22, 553
 Hatzes, A. P., Cochran, W. D., McArthur, B., et al. 2000, *ApJ*, 544, L145
 Hauschildt, P. H., Allard, F., & Baron, E. 1999, *ApJ*, 512, 377
 Itoh, Y., Oasa, Y., & Fukagawa, M. 2006, *ApJ*, 652, 1729
 Janson, M., Brandner, W., Henning, T., et al. 2007, *AJ*, 133, 2442
 Janson, M., Reffert, S., Brandner, W., et al. 2008, *A&A*, 488, 771
 Kobayashi, H., Watanabe, S., Kimura, H., & Yamamoto, T. 2008, *Icarus*, 195, 871
 Kobayashi, H., Watanabe, S., Kimura, H., & Yamamoto, T. 2009, *Icarus*, 201, 395
 Krivov, A. V., Sremčević, M., & Spahn, F. 2005, *Icarus*, 174, 105
 Krivov, A. V., Löhne, T., & Sremčević, M. 2006, *A&A*, 455, 509
 Krivov, A. V., Müller, S., Löhne, T., & Mutschke, H. 2008, *ApJ*, 687, 608
 Laor, A., & Draine, B. T. 1993, *ApJ*, 402, 441
 Li, A., & Greenberg, J. M. 1998, *A&A*, 331, 291
 Liou, J.-C., & Zook, H. A. 1999, *AJ*, 118, 580
 Liou, J.-C., Zook, H. A., & Dermott, S. F. 1996, *Icarus*, 124, 429
 Löhne, T., Krivov, A. V., & Rodmann, J. 2008, *ApJ*, 673, 1123
 Marengo, M., Megeath, S. T., Fazio, G. G., et al. 2006, *ApJ*, 647, 1437
 Marengo, M., Stapelfeldt, K., Werner, M. W., et al. 2009, *ApJ*, 700, 1647
 Moro-Martín, A., & Malhotra, R. 2002, *AJ*, 124, 2305
 Moro-Martín, A., & Malhotra, R. 2003, *AJ*, 125, 2255
 Moro-Martín, A., & Malhotra, R. 2005, *ApJ*, 633, 1150
 Mukai, T., & Fechtig, H. 1983, *Planet. Space Sci.*, 31, 655
 Müller, S., Löhne, T., & Krivov, A. V. 2010, *ApJ*, 708, 1728
 Ozernoy, L. M., Gorkavyi, N. N., Mather, J. C., & Taidakova, T. A. 2000, *ApJ*, 537, L147
 Plavchan, P., Jura, M., & Lipsy, S. J. 2005, *ApJ*, 631, 1161
 Press, W. H., Teukolsky, S. A., Vetterling, W. T., & Flannery, B. P. 1992, *Numerical recipes in C. The art of scientific computing*, 2nd edn. (Cambridge: University Press)
 Quillen, A. C., & Thorndike, S. 2002, *ApJ*, 578, L149
 Saffe, C., Gómez, M., & Chavero, C. 2005, *A&A*, 443, 609
 Soderblom, D. R., & Dappen, W. 1989, *ApJ*, 342, 945
 Song, I., Caillault, J.-P., Barrado y Navascués, D., Stauffer, J. R., & Randich, S. 2000, *ApJ*, 533, L41
 Strubbe, L. E., & Chiang, E. I. 2006, *ApJ*, 648, 652
 Vitense, C., Krivov, A. V., & Löhne, T. 2010, *A&A*, 520, A32
 Wood, B. E., Müller, H.-R., Zank, G. P., & Linsky, J. L. 2002, *ApJ*, 574, 412
 Wyatt, M. C. 2005, *A&A*, 433, 1007

² <http://www.issibern.ch/teams/exodust/>